# Topographical effects of roughness on turbulence statistics in roughness sublayer

J. Yuan[*] and M. Aghaei Jouybari

*Department of Mechanical Engineering, Michigan State University, East Lansing, Michigan 48824, USA*

Single-point turbulence statistics are compared in the roughness sublayer (RSL) of turbulent open-channel flows over smooth wall and wall roughness with different textures using direct numerical simulations (DNS). The goal is to identify how the range of scales contained in a roughness topography affects the drag generation, momentum transfer, and energy balance. The presence of large surface wavelengths is shown to reduce the overall surface slope, leading to a sparser distribution of roughness-wake regions. This may provide a physical explanation why a wider scale surface tends to produce lower friction coefficient and higher Reynolds stress anisotropy as observed previously. In addition, despite recent observations of negligible form-induced turbulent kinetic energy (TKE) productions over narrow-scale surface such as sand grains and gravel bed, it is shown that these productions can be significant over a multiscale surface. We also identify several factors crucial for these productions; they include the roughness drag coefficient, the roughness geometry function, and both micro- and macroscopic surface scales.

## I. INTRODUCTION

Wall roughness plays an important role in many fields of study. A substantial amount of work has been carried out to understand the dynamics of turbulent flows over rough walls, for both engineering and environmental applications, summarized in Refs. [1,2]. For equilibrium wall-bounded flows (such as developed channel flows and zero-pressure-gradient boundary layers) in the limit of very high Reynolds numbers, the validity of Townsend's outer-layer similarity hypothesis has been well established: outside the roughness sublayer (RSL)—the layer dynamically influenced by length scales associated with roughness—the turbulent motions in a boundary layer at high Reynolds number are independent of the wall roughness, except for the role of the wall in setting the friction velocity, $u_\tau$, and the virtual origin, $d$.

Despite the fact that the RSL does not affect the outer layer in equilibrium boundary layers, the RSL flow dynamics are important for turbulence response in many nonequilibrium wall-bounded flows, where the roughness effect may be felt throughout the boundary layer and wall similarity may not apply. For example, Ref. [3] compared a smooth wall with one roughened with sand grains in a flat-plate boundary layer subjected to strong spatial acceleration; on a smooth wall, the pressure gradient leads to rapid distortion of turbulence and quasilaminarization, but the presence of roughness leads to short turbulence timescale and eliminates quasilaminarization. As another example, Ref. [4] compared oscillatory open-channel flow over smooth and rough beds; in the accelerating stage, on the smooth wall turbulence is suppressed, while the time duration of such phenomenon dramatically reduces on a rough bed. Recent work in Ref. [5] of DNS studies of

---

[*]junlin@egr.msu.edu

rough-wall oscillatory wall-bounded flow showed that roughness modulates the near-wall turbulence and contributes to a fully developed equilibrium turbulence during the time period between the early acceleration until mid-deceleration phase, which is absent on a smooth wall [6]. These differences between smooth- and rough-wall turbulence responses were explained as a result of the modulation of turbulence by the form-induced fluctuation, also termed "wake turbulence" [7], which responds more rapidly than turbulent fluctuations to the distortion of the mean and phase-averaged flow.

The RSL transport is also an important topic for environmental and meteorological applications where fluxes of momentum and scalar—such as pollutants, heat, and biological agents—inside the RSL are of crucial importance. The form-induced fluctuations inside the RSL have been given particular attention. They affect the generation and redistribution of turbulent kinetic energy (TKE) through additional production and transport mechanisms absent in smooth-wall turbulence, leading to a "spectral short-cut" as the large-scale outer-layer flow generates eddies directly at the roughness scales. The impacts of the form-induced fluctuations were discussed for canopy flows [1,8], three-dimensional roughness geometries [9–11], and urban roughness such as idealistic cube arrays (e.g., Ref. [12]) and realistic city layouts [13]. In addition, the effect of form-induced fluctuations on RSL transport has been shown to vary with the topographical details; one observed effect of roughness texture is on the sign and magnitude of the wake production, which represents the direct energy conversion between the turbulence and the form-induced fluctuations. For example, experimental studies of flows around gravel-bed [9,14] and DNS studies of flow over sand-grain roughness [11] showed negligible wake production compared to the shear production, while for canopies the two productions typically reach similar magnitudes [8].

Understanding the link between topographical details and the RSL flow is also crucial for the modeling of the sublayer. One modeling approach is through predictive correlation of roughness drag (usually quantified by the equivalent sand-grain height, $k_s$) based on either surface characteristics or flow statistical quantities. Examples include the correlations based on moments of height distribution [15], mean surface slope [16], roughness density [17], and wall-normal turbulent fluctuations at roughness crest [18]. Understanding how the geometry affects the local time-mean flow pattern and turbulence activity is necessary for the exploration towards a universal correlation.

Though detailed analyses of the sublayer exist (see Refs. [19–22], among others), current understandings of this layer are mostly limited to roughness types that are characterized by narrow scales, while many naturally occurring surfaces such as landscape and bathymetry are usually multiscale or fractal-like [23]. The fractal roughness has been studied in Refs. [24,25] with the main focuses on relevant modeling strategies, while a theory on the fundamental aspects of its effect is yet to be established. As a first step toward this goal, this work addresses the following questions:

(1) To what extent does a wide-scale roughness affect the wall friction and the balances of mean momentum and Reynolds stresses?

(2) What roughness characteristics affect RSL processes such as various TKE production mechanisms?

## II. OBJECTIVES

Fully developed open-channel flows with two rough surfaces are compared: one synthetic sand-grain roughness (SG) that is relatively regular, and one replicated from a surface scan on a hydraulic turbine blade (TB) that is irregular and multiscale. Both cases are in the fully rough regime to eliminate the Reynolds number dependence. DNS simulations are performed with the roughness geometry well resolved using an immersed boundary method (IBM). Results are also compared to a smooth-wall baseline (SM). The governing equations, numerical methods, and parameters are described in Sec. III; Sec. IV presents results on the mean velocity, the stresses and the balances of mean momentum, and TKE. As two very texture-sensitive terms in the TKE balance, the two form-induced production terms are discussed in Sec. IV E.

## III. METHODOLOGY

### A. Governing equations

The incompressible flow of a Newtonian fluid is governed by the equations of conservation of mass and momentum:

$$\frac{\partial u_i}{\partial x_i} = 0, \tag{3.1}$$

$$\frac{\partial u_j}{\partial t} + \frac{\partial u_i u_j}{\partial x_i} = -\frac{\partial P}{\partial x_j} + \nu \nabla^2 u_j + F_j. \tag{3.2}$$

Here, $x_1$, $x_2$, and $x_3$ (or $x$, $y$, and $z$) are, respectively, the streamwise, wall-normal, and spanwise directions, and $u_j$ (or $u$, $v$, and $w$) are the velocity components in those directions; $P = p/\rho$ is the modified pressure, $\rho$ is the density, and $\nu$ is the kinematic viscosity. The term $F_j$ in Eq. (3.2) is a body force imposed by the IBM to impose no-slip boundary conditions on the rough surface, which is well resolved by the grid. The IBM method is based on the volume-of-fluid approach [26]; its detailed implementation and validation are provided in Refs. [11,27]. The $F_i$ values are non-negligible in the boundary cells of roughness only. The simulations are performed using a well-validated code that solves the governing equations (3.1) and (3.2) on a staggered grid using second-order, central differences for all terms, second-order accurate Adams-Bashforth semi-implicit time advancement, and MPI parallelization [28].

In the RSL, roughness leads to spatial heterogeneity of the time-averaged variables; these time-averaged fluctuations are separated from turbulent fluctuations using the double-averaging (DA) decomposition introduced in Ref. [7],

$$\theta(\boldsymbol{x}, t) = \langle \overline{\theta} \rangle(y) + \widetilde{\theta}(\boldsymbol{x}) + \theta'(\boldsymbol{x}, t), \tag{3.3}$$

where $\theta$ is an instantaneous flow variable, $\langle \theta \rangle$ is the intrinsic spatial average in the $(x, z)$ plane, $\langle \theta \rangle = 1/A_f \int_{A_f} \theta \, dA$ (where $A_f$ is the area occupied by fluid), $\overline{\theta}$ is the temporal average, $\theta' = \theta - \overline{\theta}$ is the instantaneous turbulent fluctuation, and $\widetilde{\theta} = \overline{\theta} - \langle \overline{\theta} \rangle$ is the form-induced fluctuation. The area averaging carried out in the total area of fluid and solid, $A_o$, is termed superficial area averaging, denoted by $\langle \theta \rangle_s = 1/A_o \int_{A_f} \theta \, dA$; the two averaging approaches satisfy the relation $\langle \rangle_s = \Phi(y) \langle \rangle$, where $\Phi(y)$ is the area fraction of fluid in the $(x, z)$ plane, or the "roughness geometry function" [29],

$$\Phi(y) = \frac{A_f(y)}{A_o}. \tag{3.4}$$

It is worth noting that the triple decomposition shown in Eq. (3.3) differs from the decomposition of Ref. [30] in that here it is not the organized motions in time, but the time-mean fluctuations in space that are subtracted from the total fluctuations.

The calculation of wall shear stress (including both viscous and pressure drag contributions) is by integrating the time-averaged IBM body force $F_1$,

$$\tau_w = \frac{\rho}{L_x L_z} \int_{\mathcal{V}} \overline{F_1}(x, y, z) \, dx \, dy \, dz, \tag{3.5}$$

where $\mathcal{V}$ represents the total simulation domain and $L_{x_i}$ is the domain size in $x_i$. For detailed explanation of this method, see Ref. [27].

### B. Rough surfaces

The two rough surfaces are shown in Figs. 1(a) and 1(b). The SG surface is formed as a uniform distribution of randomly oriented ellipsoids of the same geometry (adapted from Ref. [26]). The
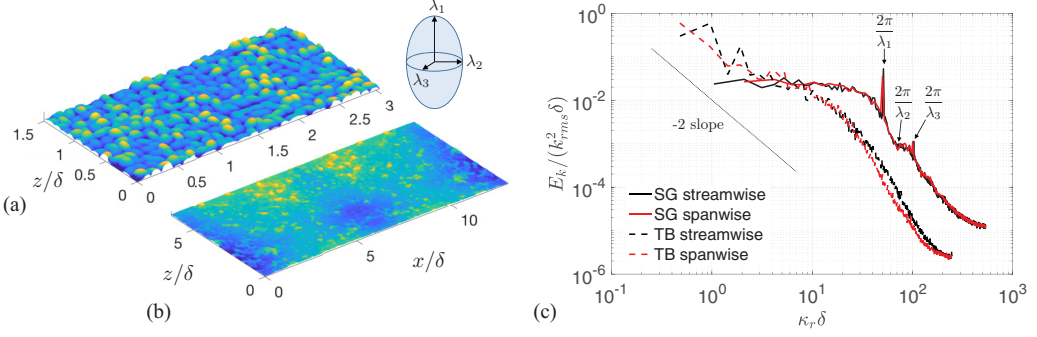
FIG. 1. Rough surfaces colored by heights of (a) one quarter of SG surface and (b) one half of TB surface. (c) Power spectra of height fluctuations with wave number $\kappa_r$ in $x$ and $z$.

three semiaxes $\lambda_1$, $\lambda_2$, and $\lambda_3$ (ordered from longest to shortest) satisfy the ratio $1 : 0.7 : 0.5$; the spacing between neighboring ellipsoids approximately equals to $\lambda_1$ in all directions. The TB surface is replicated from a hydraulic turbine blade (same as surface S4 studied in Ref. [31]), containing horizontal surface scales larger than the boundary layer thickness, $\delta$ (i.e., the channel half height). The initial turbine scan is mirrored in both $x$ and $z$ to produce the final surface that satisfies the periodic conditions.

The characteristic parameters for the two surfaces are compared in Table I. The origin of $y$ axis is defined at the lowest roughness trough of each surface. The two surfaces share the same first-order moment of height fluctuations, $\text{Ra} = 0.016\delta$, similar crest heights (equivalent to the peak-to-trough height), $k_c \approx 0.1\delta$, similar root-mean-square, $k_{\text{rms}}$, and kurtosis, $k_u$ (close to 3.0, indicating almost random surface height distribution), and are both peaky (skewness, $s_k > 0$). But they differ significantly in the averaged surface slope magnitude, as shown by the effective slopes (ES) in $x$ and $z$ [16],

$$\text{ES}_{x_i} = \frac{1}{L_x L_z} \int_{L_x, L_z} \left| \frac{\partial k(x, z)}{\partial x_i} \right| dx dz, \tag{3.6}$$

where $k(x, z)$ is the local surface height; ES values for TB are around $1/4$ of those for SG, in both $x$ and $z$.

The power spectra of height fluctuations are compared in Fig. 1(c). The overall TB spectrum is comparable to a power-law distribution with a slope of $-2$, indicating similarity to a fractal roughness. For SG, however, the spectral decay occurs only for scales smaller than the grain size; spectral peaks are present at the characteristic grain dimensions, i.e., the semiaxis lengths. The comparison shows that the two surfaces differ significantly in the scales of prominent surface fluctuations.

The probability density functions (PDF) of the local surface gradients in $x$ and $z$ are shown in Fig. 2. Steep gradients (higher than around 0.25, or $14°$ inclination from a wall-parallel plane) occur more frequently for SG than for TB. As a result, one expects more dominant local separation in the RSL for SG, and, consequently, a higher pressure drag. The difference between the $x$- and $z$-gradient distributions is negligible, suggesting that the two roughness textures are free of any predominant

TABLE I. Characteristic parameters of the surfaces.

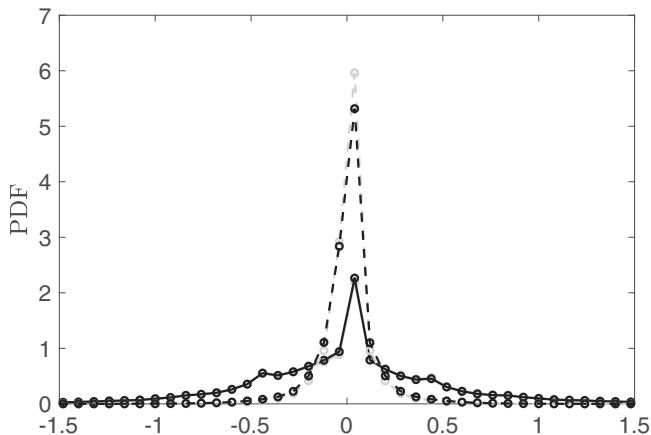| Surface | $k_c/\delta$ | $\text{Ra}/\delta$ | $k_{\text{rms}}/\text{Ra}$ | $s_k$ | $k_u$ | $\text{ES}_x$ | $\text{ES}_z$ |
|---------|-------------|---------------------|-----------------------------|-------|-------|---------------|---------------|
| SG      | 0.09        | 0.014               | 1.05                        | 0.48  | 2.97  | 0.43          | 0.44          |
| TB      | 0.12        | 0.014               | 1.17                        | 0.20  | 3.49  | 0.10          | 0.08          |

FIG. 2. Probability density functions of local surface gradients, $\partial k/\partial x$ (black) and $\partial k/\partial z$ (gray), for SG (—) and TB (– – –) roughness.

direction. The milder overall slope for TB is due to the presence of larger surface wavelengths while the single-point moments of surface height are to be kept constant.

### C. Simulation parameters

The parameters of all cases are listed in Table II. The Reynolds number $\mathrm{Re}_\tau = u_\tau \delta/\nu = 1000$ for all cases. The critical value of the roughness Reynolds number $(k_s^+)$ corresponding to the start of the fully rough regime for these surfaces were found as around 80 and 20 for SG and TB, respectively [31]; the current $k_s^+$ values indicate fully rough regime for both cases. The virtual origin, $d$, is defined as the centroid of the wall-normal profile of the time- and space-averaged total drag distribution [32].

The roughness sublayer thickness, $y_R$, is defined as the location where $\langle \widetilde{u}^2 \rangle^{1/2}$ reaches $0.06\langle \overline{u} \rangle$, similar to that in Ref. [33]; above this location, the spatial variation of $\widetilde{u}$ reduces below the threshold value, and the flow is considered not dynamically influenced by roughness length scales. Here, $y_R/k_s = 1.5$ and 5.8 for SG and TB, respectively. These values match marginally with the range commonly observed in the literature, which is 2–5 times the characteristic height ($k_s$ or $k_c$). Evidence has shown that a larger separation of distributed roughness elements tends to thicken the RSL [34,35]. This is consistent with the current observation, as TB shows significantly larger horizontal separation between the tall protuberances compared to SG due to the large surface undulations.

An overall roughness drag coefficient $C_{d,R}$ can be defined as $\tau_w$ normalized by the velocity immediately outside the roughness wake region, $U_R = \langle \overline{u} \rangle|_{y_R}$,

$$C_{d,R} \equiv \frac{\tau_w}{1/2\rho U_R^2} = \frac{2}{(U_R^+)^2}. \tag{3.7}$$

TABLE II. Case summary. Superscript $+$ indicates normalization in wall units ($u_\tau$ and viscous length scale, $\delta_\nu = \nu/u_\tau$).

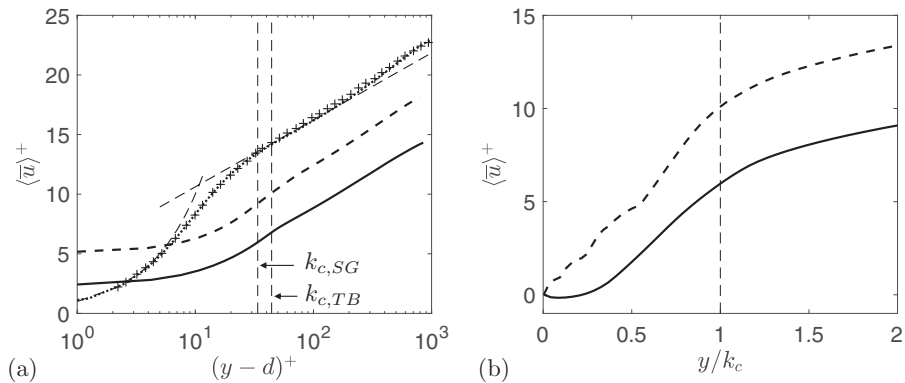| Surface | $\mathrm{Re}_\tau$ | $k_s^+$ | $d/\delta$ | $y_R/\delta$ | $C_{d,R}$ | $(L_x, L_z)/\delta$ | $(n_i, n_j, n_k)$ | $(\Delta x^+, \Delta y_{\min}^+, \Delta z^+)$ |
|---|---|---|---|---|---|---|---|---|
| SM | 1000 | | | | | (6,3) | (512, 256, 512) | (11.7, 0.3, 5.8) |
| SG | 1000 | 78 | 0.044 | 0.12 | 0.031 | (6,3) | (1024, 236, 512) | (6.0, 0.7, 6.0) |
| TB | 1000 | 24 | 0.058 | 0.14 | 0.015 | (13,13) | (1024, 259, 1024) | (13.0, 0.8, 13.0) |

FIG. 3. DA velocity against (a) logarithmic and (b) linear $y$ coordinates. --- SM, —— SG, and $---$ TB. + Smooth-wall experiment [37]. Thin dashed lines indicate crest locations.

$C_{d,R}$ characterizes the surface resistance to the overlying flow in the RSL. It has been shown in Ref. [3] that for a turbulent boundary layer with strong spatial acceleration of the free stream, $C_{d,R} = $ const. as long as the flow is in the fully rough regime. This is because the RSL flow stays in equilibrium regardless of the varying outer layer. In contrast, an alternative coefficient definition using the free-stream velocity (i.e., $C_f$) varies during the acceleration. This indicates that $C_{d,R}$ has merits in characterizing the wall friction in a fully rough, nonequilibrium wall turbulence. Note that $C_{d,R}$ becomes Reynolds number dependent in the transitionally rough regime and is ill defined on a smooth wall. Here, it is found that the TB roughness produces a much lower $C_{d,R}$ than SG (Table II), which will be discussed in Sec. IV A.

The domain sizes in $x$ and $z$ are $(6\delta, 3\delta)$ for SM and SG, while $(13\delta, 13\delta)$ for TB; a larger domain is required for TB to accommodate larger surface wavelengths. $n_i$, $n_j$, $n_k$ are the numbers of grid points in $x$, $y$, $z$. The mesh is uniform in $x$ and $z$ but refined near the wall in $y$, with three grid points below $y^+ = 1$ for SM, and $\Delta y^+ < 1$ in the layer below roughness crest for both rough cases. The grid size normalized by the Kolmogorov length, $\eta$, is 6–11 in $x$ and $z$, and much smaller in $y$. For a curved channel flow, scales less than $15\eta$ were found to contribute to most of the dissipation [36]. Thus, the current spatial resolution is considered sufficient.

Only a half channel is simulated. No-slip and symmetric conditions are applied to the bottom and top boundaries of the simulation domain, respectively; periodic conditions are used in $x$ and $z$. A constant pressure gradient is applied to drive the flow. Data are collected for a simulation time of $T \approx 50\delta/u_\tau$ (where $u_\tau$ is the friction velocity) after the transient.

## IV. RESULTS

### A. DA velocity and pressure-drag generation

The semilog plots of $\langle \overline{u} \rangle$ profiles are compared in Fig. 3(a). The smooth-wall profile collapse well with experimental measurement of a channel flow with the same $\mathrm{Re}_\tau$ [37]. The two rough surfaces yield significantly different roughness function, $\Delta U^+$—defined as the mean velocity offset in the logarithmic region from the smooth-wall profile; this is consistent with the higher $k_s^+$ and $C_{d,R}$ values for SG. An explanation for the higher drag on SG is that the pressure drag is mostly generated by peaky surface structures with sufficiently high local slope; these structures are less densely distributed in TB geometry. Indeed, the spatial perturbations of time-mean surface pressure (Fig. 4) display a sparser distribution of regions with intense negative $x$ gradients (indicator of pressure drag) on TB. This may explain previous observations that the large surface wavelengths tend to reduce drag generation on fractal surface [25] and realistic roughnesses [31,38].
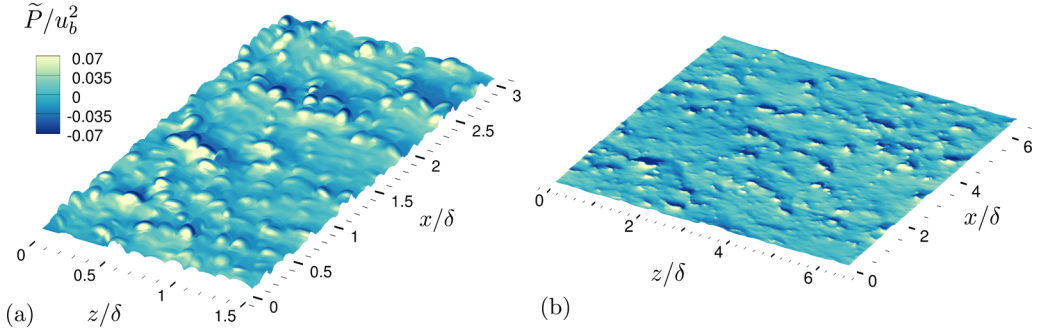
FIG. 4. Rough surfaces colored by time-mean surface pressure perturbation for (a) SG and (b) TB. Partial domain is shown for clarity. Normalization is done using bulk velocity, $u_b = 1/\delta \int \langle \overline{u} \rangle dy$.

The rough-wall $\langle \overline{u} \rangle$ profiles on linear scale [Fig. 3(b)] manifest a close-to-linear profile for a considerable range below the crest. This is different from an exponential velocity profile with an inflection point at the crest, as commonly observed for canopies (see, e.g., Ref. [1]) and distributed cubical roughness [19,39]. Reference [40] showed that a monotonically increasing $\Phi(y)$ as the crest is approached—such as the present cases—may lead to a linear velocity profile, while an exponential profile can be associated with a constant $\Phi$. Similar linear profiles are also observed for other types of roughness with $d\Phi(y)/dy > 0$ such as gravel-bed roughness [9] and spherical segments [29].

## B. Reynolds and dispersive stresses

The normal and shear components of the Reynolds stress tensor are shown in Fig. 5(a). Wall similarity is demonstrated outside the RSL. Inside the RSL, noticeable differences are observed between the rough cases: TB leads to stronger streamwise component of the normal stresses and weaker values in the other two normal components compared to SG. These differences are more clearly shown in Fig. 5(b) using the anisotropy of the Reynolds stress tensor (no summation over Greek index),

$$b_{\alpha\alpha} = \frac{\langle \overline{u'_\alpha u'_\alpha} \rangle}{\langle \overline{u'_i u'_i} \rangle} - \frac{1}{3}. \tag{4.1}$$
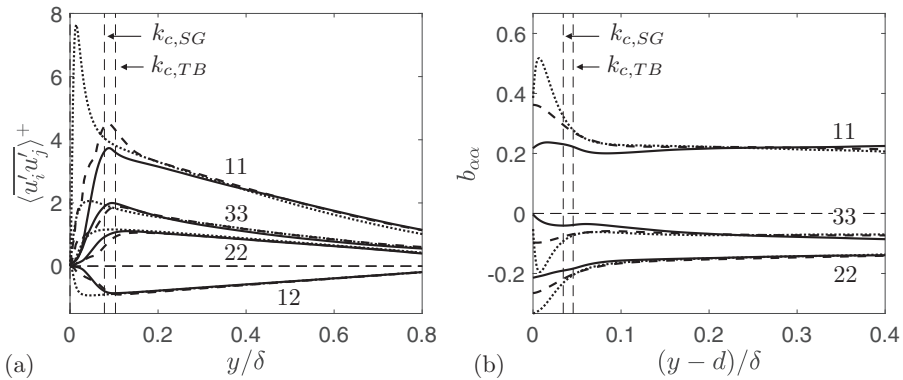


FIG. 5. Tensor components of (a) Reynolds stress and (b) its anisotropy. --- SM, —— SG, −−− TB.
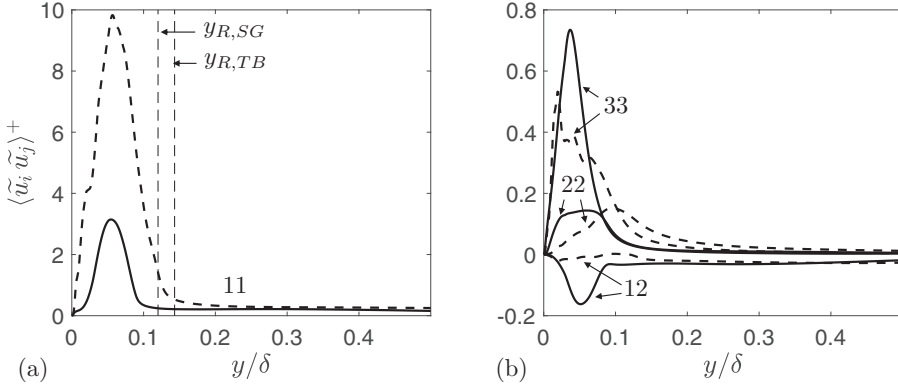
FIG. 6. Tensor components of dispersive stress. —— SG; − − − TB.

Near the wall, both rough cases lead to more isotropic TKE distribution among the three directions compared to the smooth case; this is consistent with common observations in the literature. Between the two rough cases, TB gives a higher fraction of TKE resting in $u'$. Such difference in anisotropy can be attributed to the topographical effect on TKE redistribution by the pressure work (see Sec. IV D).

The normal and shear components of the dispersive stress tensor are shown in Fig. 6. The TB surface leads to more anisotropic dispersive fluctuations, with more intense $\widetilde{u}$ and weaker $\widetilde{w}$. In addition, the dispersive shear stress, $\langle \widetilde{u}\widetilde{v} \rangle$, is significant for SG, but negligible for TB. Thus, the wall-normal momentum transfer by the form-induced velocities depends very sensitively on the textural details.

To explain the differences in dispersive stresses, the distributions of $\widetilde{u}_i$ inside the RSL is shown in Fig. 7 in the wall-parallel plane at $y = d$; this elevation is close to the peaks of various dispersive stress components in Fig. 6. On TB, higher magnitudes of positive $\widetilde{u}$ are produced in the large regions corresponding to the troughs of long-wavelength surface undulations along $x$; such phenomenon is absent in SG. For $\widetilde{v}$ and $\widetilde{w}$, the peak magnitudes appear similar between the two surfaces, but the regions of such intense fluctuations occur less frequently for TB. It is possibly because that the more prevalent surface undulations in TB lead to weaker $\widetilde{v}$ and $\widetilde{w}$ from the continuity of $\widetilde{u}_i$ field. In addition, for TB the large surface wavelengths in $z$ lead to wake regions (negative $\widetilde{u}$) with similarly large spanwise scales. These wide wake regions tend to persist for a long distances downstream and shadow lower surface structures along the way, contributing to a lower form drag.

The drastic difference in the dispersive shear stress can be explained using the joint PDFs of $\widetilde{u}$ and $\widetilde{v}$ inside the RSL (Fig. 8). Quadrant contributions in analogy to those of turbulent fluctuations [41] are analyzed. The joint PDF for SG displays an inclined distribution pattern with more intense events in Q2 and Q4 than those in Q1 and Q3, leading to non-negligible, negative $\langle \widetilde{u}\widetilde{v} \rangle$. For TB, the strongest $\widetilde{u}$ fluctuations in both signs are more intense than those for SG, but the distribution of $\widetilde{v}$ values are almost symmetric with respect to the $\widetilde{v} = 0$ line, yielding a negligible spatial average of $\widetilde{u}\widetilde{v}$. Such difference is precisely due to the role of large surface scales. For SG, regions with $\widetilde{u} < 0$ are mostly associated with the upstream portion of a recirculation region behind a surface protuberance where $\widetilde{v} > 0$ (upward flow), and regions with $\widetilde{u} > 0$ mostly appear in elongated region of downward flow at the end of the recirculation, where $\widetilde{v} < 0$. Negative dispersive shear stress values were also observed associated with the mean recirculation for cube roughness [42] and gravel bed [43]. In contrast, for TB roughness the regions with intense $\widetilde{u}$ in both signs are not distinctively associated with the recirculation phenomenon, but instead with the large-scale surface undulations.
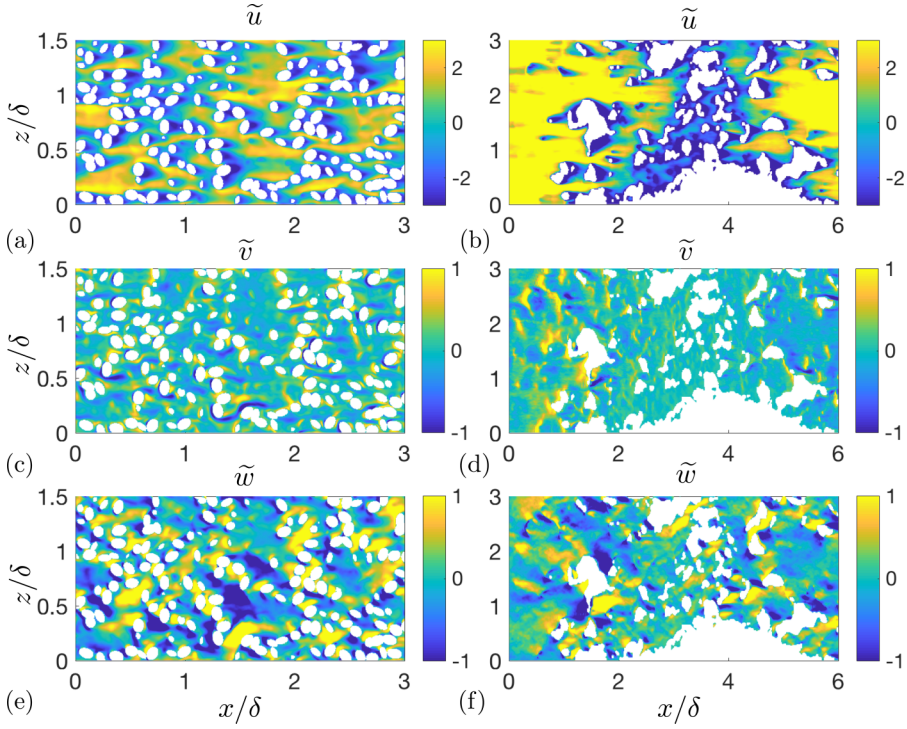
FIG. 7. Form-induced fluctuations in plus units for SG [(a), (c), (e)] and TB [(b), (d), (f)] in the wall-parallel plane at $y/d = 1$. White region is within solid.

## C. Mean momentum balance

The aforementioned differences in the stresses suggest a change in the mean momentum balance inside the RSL, which is analyzed here. The streamwise DA momentum equation is [7,9]

$$-\frac{\partial \langle \overline{P} \rangle_s}{\partial x} - \frac{\partial \langle \overline{u'v'} \rangle_s}{\partial y} - \frac{\partial \langle \widetilde{u}\, \widetilde{v} \rangle_s}{\partial y} + \nu \frac{\partial^2 \langle \overline{u} \rangle_s}{\partial y^2} + f_v + f_p = 0, \qquad (4.2)$$
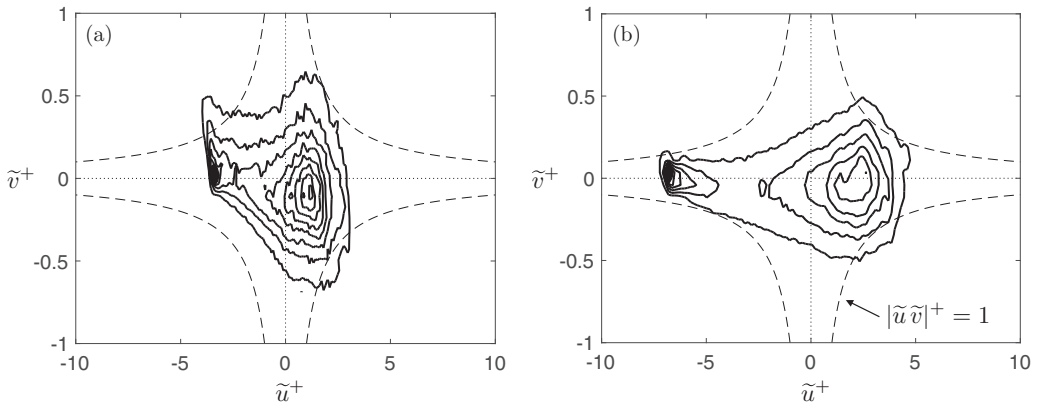


FIG. 8. Joint probability density function of $\widetilde{u}$ and $\widetilde{v}$ for (a) SG and (b) TB at $y/d = 1$. Contour line values (in wall units) range from 0.05 to 0.5 with step size 0.05.
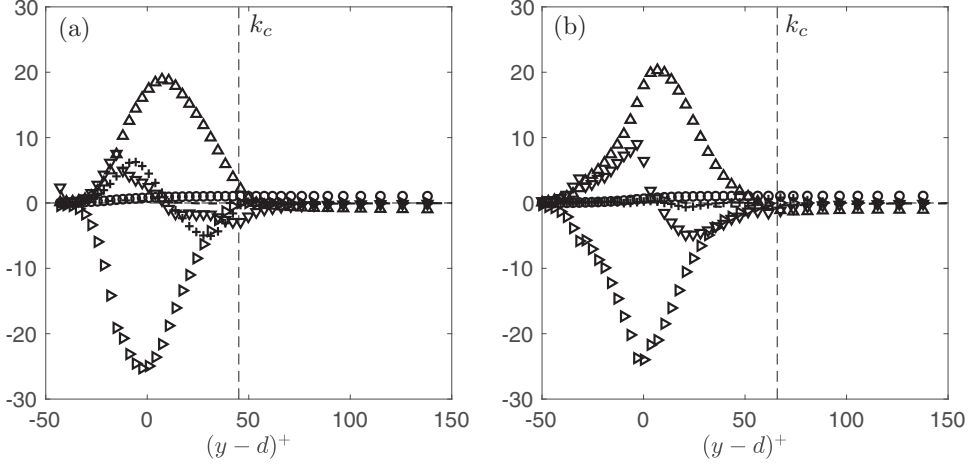
FIG. 9. Mean momentum balance for (a) SG and (b) TB, normalized in wall units. Symbols: $\bigcirc$, pressure gradient; $\triangledown$, viscous force; $\triangle$, turbulence inertia; $+$, dispersive term; $\triangleright$, total drag; and $---$, residual.

where

$$f_\nu = \nu \langle \nabla^2 \widetilde{u} \rangle_s \tag{4.3}$$

and

$$f_p = \left\langle \frac{\partial \widetilde{P}}{\partial x} \right\rangle_s \tag{4.4}$$

are the viscous and pressure components of the total drag, respectively. Instead of calculating $f_p$ and $f_\nu$ individually, the local sum of viscous and pressure drags is obtained as the time- and space-averaged $F_1$. The wall-normal profiles of the terms in Eq. (4.2) are plotted in Fig. 9. For both rough surfaces, the turbulence inertia transfers outer-layer mean momentum down to the RSL to counter the sink due to the total drag; the excessive mean momentum at the top half of the RSL is then transferred downward through both viscous and dispersive stresses. The dispersive term is of a similar magnitude as the viscous term for SG, while negligible for TB. Nevertheless, the nature of the balance does not appear to be texture sensitive, due to the relatively weak magnitude of the dispersive shear stress itself.

### D. Energy balance

The budgets of the normal Reynolds stresses, $\langle \overline{u_\alpha'^2} \rangle_s$ can be written similar to those in Ref. [9] as

$$0 = \left[ \underbrace{-2\langle \overline{u_\alpha' v'} \rangle_s \frac{\partial \langle \overline{u}_\alpha \rangle}{\partial y}}_{P_s} + P_w + P_m \right] \underbrace{- \left\langle \frac{\partial}{\partial x_j} \widetilde{u_\alpha' u_\alpha'} \widetilde{u}_j \right\rangle_s}_{T_w} \underbrace{- \left\langle \frac{\partial}{\partial x_j} \overline{u_\alpha' u_\alpha' u_j'} \right\rangle_s}_{T_t}$$

$$\underbrace{-2 \left\langle \overline{u_\alpha' \frac{\partial P'}{\partial x_\alpha}} \right\rangle_s}_{\Pi} \underbrace{+\nu \left\langle \frac{\partial^2 \overline{u_\alpha'^2}}{\partial x_j \partial x_j} \right\rangle_s}_{T_\nu} \underbrace{-2\nu \left\langle \overline{\frac{\partial u_\alpha'}{\partial x_j} \frac{\partial u_\alpha'}{\partial x_j}} \right\rangle_s}_{\epsilon}, \tag{4.5}$$

where the terms on the right-hand side are, respectively, shear production ($P_s$), additional productions due to the form-induced shear ($P_w$ and $P_m$), transport due to wake fluctuations ($T_w$), turbulent transport ($T_t$), viscous transport ($T_\nu$), pressure work ($\Pi$), and viscous dissipation ($\epsilon$). $P_m$ and $P_w$ are

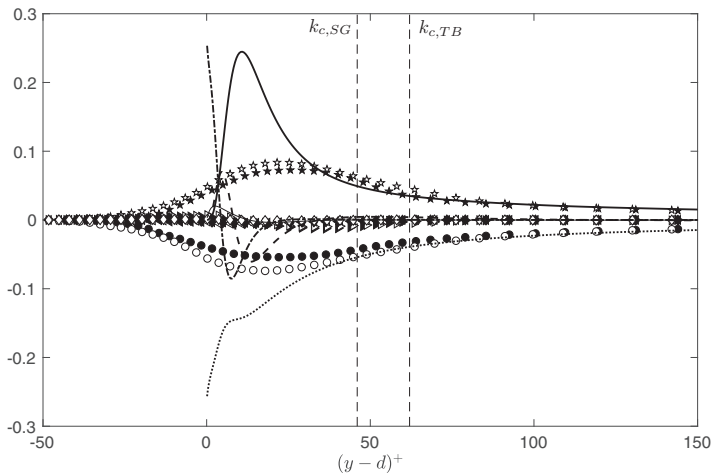FIG. 10. TKE budget terms in wall units for SM (lines), SG (filled symbols), and TB (empty symbols). Lines: ——, $P_s$; −−−, $T_t$; −·−, $T_v$; —— (thin), $T_p$; ---, $\epsilon$. Symbols: $\star$, $(P_s + P_w + P_m)$; $\triangleright$, $T_t$; $\triangleleft$, $T_v$; $\diamond$, $T_p$; $\bigcirc$, $\epsilon$.

discussed in details in Sec. IV E. Note that, in calculating the spatial averaging in the present IBM framework, the interface cells are not included. If the interface cells are also included, an additional term $2\langle \overline{F'_\alpha u'_\alpha} \rangle_s$—with a small magnitude of 4% of $P_s$ peak value—appears due to the IBM body force, but the nature of the balance is not affected. For the smooth case, Eq. (4.5) still applies with the form-induced terms $P_m$, $P_w$ and $T_w$ equal to zero.

Summing over the three components yields the budget of the TKE, whose terms are shown in Fig. 10, normalized by wall units. Note that the sum of three $\Pi$ components gives the pressure transport, $T_p$. The residuals are around 2% of $P_s$, which is considered negligible. Above the RSL, the two rough cases agree well with the smooth case, expected from wall similarity. Inside the RSL, the balances share similarities with the one across the mixing layer created by a backward-facing step [44], presumably as a result of the local shear layers associated with the roughness wake. Specifically, the peak locations of production and dissipation coincide away from the wall, and turbulent transport removes excessive energy from the elevation of maximum production and transfers it toward the wall. The transport due to wake fluctuations and viscosity are negligible. For gravel-bed roughness, Ref. [9] observed a similar balance, with a peak of production at $y/k_c \approx 0.8$. The current results show a similar peak location of $0.77k_c$ for SG, but $0.60k_c$ for TB. Variation in roughness texture herein does not appear to fundamentally modify the mixing-layer dynamics; instead, it affects the averaged elevation of the local shear layers relative to the crest height.

Next, the wall-normal Reynolds stress balance (Fig. 11) is discussed as its intensity at the crest level has been shown to demonstrate significant sensitivity to texture. The productions of $v'$ energy are nonzero in rough cases due to $P_w$. A significant difference between the two textures is that the fraction of TKE redistributed to $v'$ through the pressure work is much lower around TB; interestingly, $\Pi_{22}$ reduces to a negligible level near the virtual origin. Such weakened pressure work is compensated by an increase in turbulent transport (not shown), indicating a clear structural change of turbulence.

Figure 12 visualizes the instantaneous pressure work against $v'$, whose time-and-space average yields $\Pi_{22}$. The contours are shown in the wall-parallel plane at $(y - d)^+ \approx 25$, in the elevation where $\Pi_{22}^+$ differs by around 50% between the two rough cases. It is evident that regions with a high intensity of spatially intermittent pressure work ($v'^+ \partial P'^+/\partial y^+ \geqslant 0.1$) correspond mostly to the high-slope, tall protuberances (or a cluster of them). This is presumably because of the form-induced shear ($\partial \widetilde{u}_i/\partial x_j$) formed in the vicinity of these surface elements, which contributes to the source in
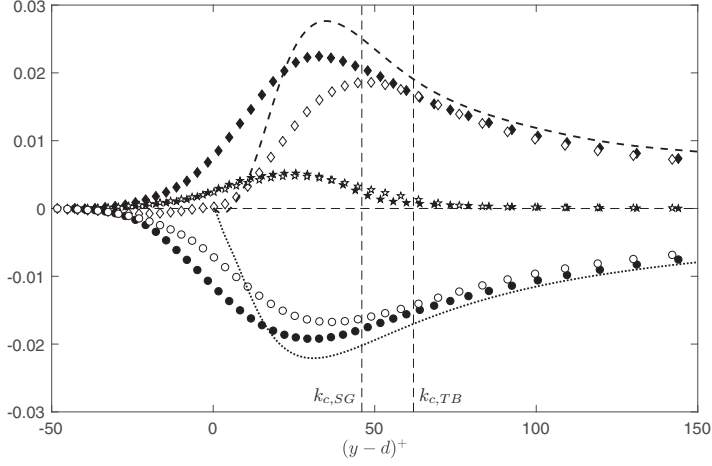
FIG. 11. Budget terms of wall-normal Reynold stress in wall units. For legend Lines: ---, $\epsilon$; $---$, $\Pi$. Symbols: $\star$, $P_w$; $\diamond$, $\Pi$; $\bigcirc$, $\epsilon$.

the $P'$ Poisson equation (see Eq. (3.9) in Ref. [3]), or because of the intense mixing-layer turbulence activity in the wake regions. For TB, the sparser distribution of such protuberances leads to lower $\Pi_{22}^+$. The dependence of both the $v'^+$ generation and the pressure drag on the peaky protuberances lends support to the correlation between roughness drag and crest-level $v_{\text{rms}}^+$, as observed for a wide range of roughness [18,22].

### E. Form-induced turbulence productions

The additional production terms $P_m$ and $P_w$ in the rough cases are associated with the vortex stretching by the form-induced shear,

$$-2\left\langle \overline{u'_\alpha u'_j} \frac{\partial \widetilde{u}_\alpha}{\partial x_j} \right\rangle_s = \underbrace{-2\left\langle \widetilde{\overline{u'_\alpha u'_j}} \frac{\partial \widetilde{u}_\alpha}{\partial x_j} \right\rangle_s}_{P_w} \underbrace{-2\langle \overline{u'_\alpha u'_j} \rangle \left\langle \frac{\partial \widetilde{u}_\alpha}{\partial x_j} \right\rangle_s}_{P_m} . \tag{4.6}$$
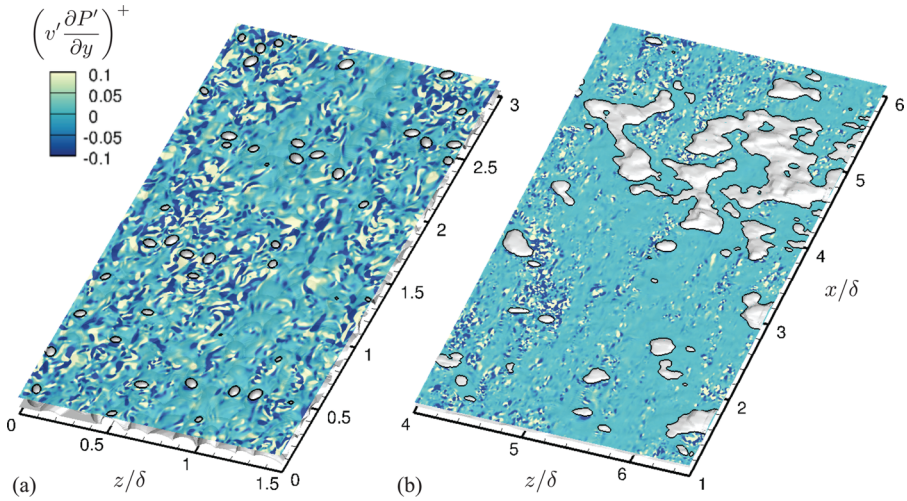


FIG. 12. Instantaneous rate of work of pressure fluctuations against wall-normal velocity fluctuations at $(y - d)^+ = 25$ on (a) SG and (b) TB. Roughness surfaces are shown in white.
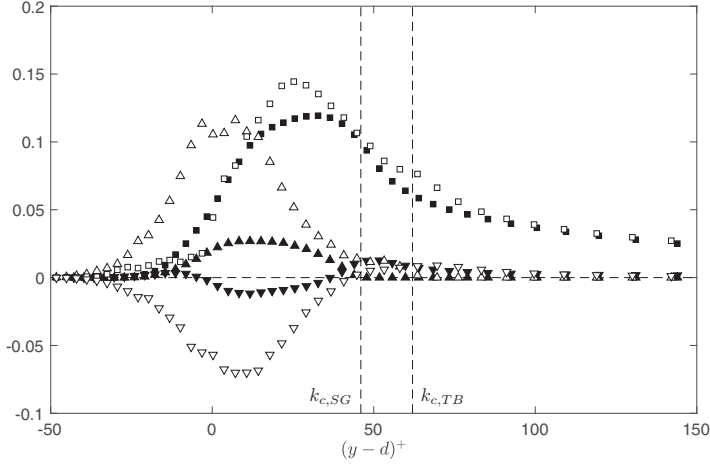
FIG. 13. Breakdown of total production of streamwise Reynolds stress for SG (filled symbols) and TB (empty symbols). Symbols: $\square$, $P_s$; $\triangle$, $P_m$; $\nabla$, $P_w$.

The portions due to $\widetilde{u'v'}_s$ and $\langle \overline{u'v'} \rangle$ are represented by $P_w$ and $P_m$, respectively. Despite largely similar total TKE productions between the two rough cases (Fig. 10), the individual production processes can be drastically different. Consider the balance of streamwise Reynolds stress, in which the majority of the TKE production resides. Figure 13 compares the three production terms between the rough cases. The profiles of $P_s$ essentially scale with wall units, due to its dependence on $\langle \overline{u'v'} \rangle$. For TB, there is an additional bump of $P_s$ at $k_c$, which might be attributed to the few tallest protuberances. Although Ref. [9] reported that the terms in $P_m$ and $P_w$ involving the vertical derivatives (the only ones that can be calculated from available experimental data) contributed to less than 5% of the total TKE production, the current results show that this may not be the case for a fractal-like surface; $P_m$ and $P_w$ may individually reach magnitudes comparable to that of $P_s$. However, $P_m$ and $P_w$ take opposite signs, leading to a smaller, less-varying sum. The contributing factors to $P_m$ and $P_w$ are discussed in the following.

First, $P_m$ is produced by the spatial-averaged form-induced shear, $\langle \partial \widetilde{u}_i / \partial x_j \rangle_s$, which varies with DA velocity in the RSL and depends on the $\Phi(y)$ variation [45],

$$\left\langle \frac{\partial \widetilde{u}_i}{\partial x_j} \right\rangle_s = \langle \overline{u}_i \rangle \frac{d\Phi(y)}{dy}. \tag{4.7}$$

Therefore, $P_m$ in the TKE budget can be recast as

$$P_{m,ii} = -2\langle \overline{u'v'} \rangle \langle \overline{u} \rangle \frac{\partial \Phi}{\partial y}. \tag{4.8}$$

Note that $P_{m,22} = P_{m,33} = 0$ as $\langle \overline{v} \rangle = \langle \overline{w} \rangle = 0$. In the limiting case with a constant $\Phi$ along $y$, such as vegetation canopies and wall-mounted cubes, $P_m$ is zero. For the current rough surfaces, both $\langle \overline{u}_i \rangle$ and the varying $\Phi(y)$ play a role in determining the $P_m$ value. The contributing factors in Eq. (4.8) are compared in Fig. 14. The drastically higher $P_m$ values for TB is mostly attributed to the higher $\langle \overline{u} \rangle^+$ due to a lower $C_{d,R}$, as well as the peak of $d\Phi/dy$ being at a higher location where the mean velocity and Reynolds shear stress are appreciable.

Next, the $P_w$ term is analyzed. Its contours for the three normal Reynolds stresses, $P_{w,\alpha\alpha}$, are compared in the wall-parallel plane at $y = d$ in Fig. 15. Regardless of texture, the local values of $P_w$ (especially the 11 and 33 components) are highly intermittent—capable of reaching over 0.1 in
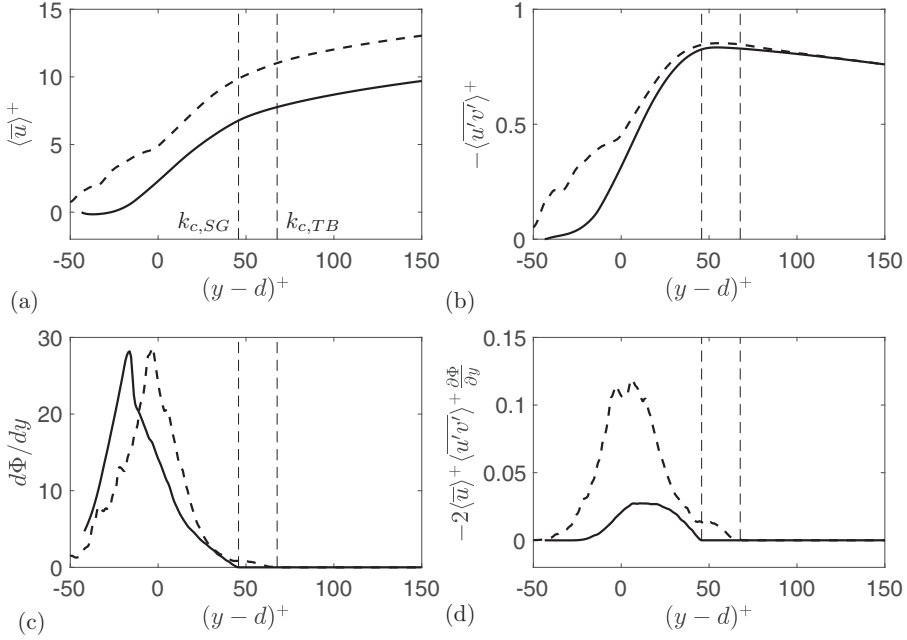
FIG. 14. [(a)–(c)] Contributing factors to (d) $P_m$ for the rough cases. —— SG, --- TB.

plus units—and the overall magnitudes are higher for the 11 component. On TB, $P_{w,11}$ demonstrates both large and small scales connected to the scale distribution of the surface, while the other two components are predominantly associated with small surface scales.

Each $P_{w,\alpha\alpha}$ consists of three terms,

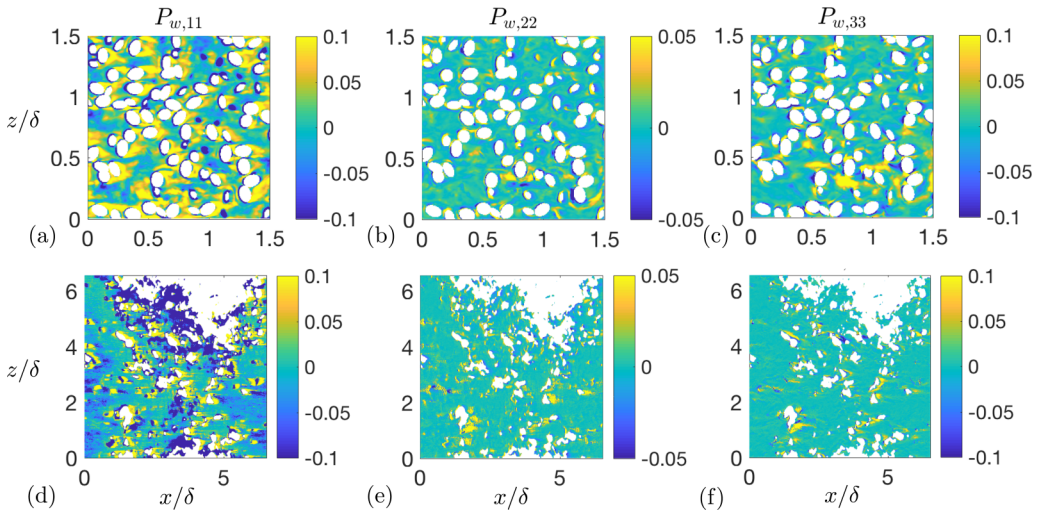$$P_{w,\alpha\alpha} = P_{w,\alpha\alpha,1} + P_{w,\alpha\alpha,2} + P_{w,\alpha\alpha,3}, \tag{4.9}$$



FIG. 15. Components of $P_w$ for SG [(a)–(c)] and TB [(d)–(e)] in wall-parallel plane at $y = d$, in wall units. White region is within solid.
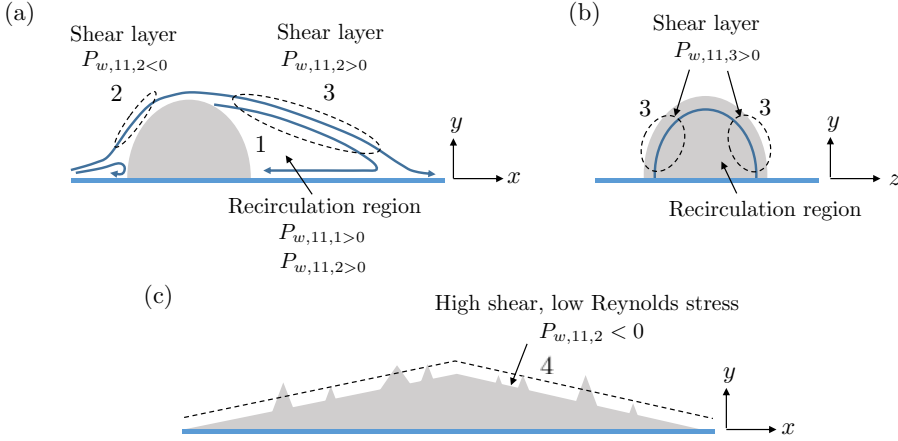
FIG. 16. Sketches of local flow characteristics to explain $P_{w,11}$ distribution in Figs. 15(a) and 15(d): Typical flows around an isolated protuberance in (a) $(x, y)$ plane and (b) $(y, z)$ plane (viewed towards $+x$ direction, and (c) over a large-wavelength surface undulation. Numbers 1–4 indicate flow characteristics discussed in text.

where

$$P_{w,\alpha\alpha,\beta} = -2\left\langle \widetilde{u'_\alpha u'_\beta} \frac{\partial \widetilde{u}_\alpha}{\partial x_\beta} \right\rangle_s.$$

(4.10)

Each term is determined by the three-dimensional distributions of two flow quantities, $\widetilde{u'_\alpha u'_\beta}$ and $\partial \widetilde{u}_\alpha / \partial x_\beta$. Thus, to fully explain the $P_w$ distribution, one needs to analyze the spatial distributions of 18 quantities, which is beyond the scope of this paper. Here, we focus on the most intensive component—$P_{w,11}$—and look for general connections between the surface geometry and the pattern of each term in Eq. (4.9).

To explain the flow patterns, one may generalize the previous findings on an isolated, wall-mounted obstacle of standard geometries to the isolated tall protuberances (or their clusters) herein. For an idealized obstacle such as a hemisphere, a cube, etc., several flow features are established [46–49]. First, a horseshoe vortex system is generated upstream of the obstacle below the stagnation point due to the adverse pressure gradient. Past the stagnation point, an attached shear layer is formed upstream of the obstacle. A mean recirculation region exists behind the obstacle, wrapped by a three-dimensional shear layer; turbulence grows inside the shear layer through Kelvin-Helmholtz instability. These features are summarized in Figs. 16(a) and 16(b).

For the present irregular surfaces, the characteristics of $P_{w,11,\beta}$ inside the RSL are conjectured based on the above-mentioned flow features, and sketched in Fig. 16. Together, they provide a gross explanation of the $P_{w,11}$ contours in Figs. 15(a) and 15(d).

*Characteristic 1.* Inside the downstream recirculation [Fig. 16(a)], $\overline{u'^2}$ and $\overline{u'v'}$ are near zero, i.e., $\widetilde{u'^2} < 0$ and $\widetilde{u'v'} > 0$ (note that $\langle \overline{u'v'} \rangle$ is negative); also, $\partial \widetilde{u} / \partial x > 0$ as the local flow accelerates in $x$, and $\partial \widetilde{u} / \partial y < 0$ (i.e., milder local mean shear inside the separation region relative to the spatial average) due to the inflection point of the $\overline{u}$ profile inside the shear layer. These phenomena lead to positive values of both $P_{w,11,1}$ and $P_{w,11,2}$.

*Characteristic 2.* In the upstream attached shear layer [Fig. 16(a)], $\partial \widetilde{u} / \partial y > 0$ as the local mean shear is steeper than the spatial average, and $\widetilde{u'v'} > 0$ as $\overline{u'v'}$ is positive or near zero; as a result, $P_{w,11,2} < 0$. Such $\overline{u'v'}$ behavior is probably due to the attenuation of $v'$ fluctuations normal to the inclined surface. For flow over staggered array of cube elements, Ref. [42] also observed positive values of $\overline{u'v'}$ immediately upstream of the cubes.

*Characteristic 3.* The three-dimensional shear layer is associated with stronger local mean shear and Reynolds shear stress than their plane-averaged values. As a result, at the top of the recirculation [Fig. 16(a)], $\partial \widetilde{u}/\partial y > 0$ and $\widetilde{u'v'} < 0$, and thus $P_{w,11,2} > 0$; at the sides of this region [Fig. 16(b)], both $\partial \widetilde{u}/\partial z$ and $\widetilde{u'w'}$ change sign moving from one side to the other, leading to positive $P_{w,11,3}$ on both sides.

*Characteristic 4.* For TB, a mild-slope, long-wavelength surface undulation forms a thin fluid layer above, following their contour [Fig. 16(c)]; this layer is characterized by steeper local mean shear compared to the average ($\partial \widetilde{u}/\partial y > 0$) and damped Reynolds shear stress due to the proximity of the surface ($\widetilde{u'v'} > 0$); together, they yield negative $P_{w,11,2}$ values.

In general, characteristics 1–3 apply to flows around local surface structures with steep slopes, where separation occurs; for SG, these are the dominant events, with the positive and negative $P_w$ contributions almost canceling out. For TB, characteristic 4 is prominent, contributing to a significant negative spatial average. These observations show that both large and small surface structures play a role in determining the averaged $P_w$ value.

## V. CONCLUSIONS

The dynamics of the roughness sublayer are important in setting the friction velocity scale for the boundary layer above and in modulating the turbulence response to mean distortions. In this work, the role of roughness texture in affecting the single-point statistics of turbulence in this layer is investigated based on DNS data of developed open-channel flows over a synthetic sand-grain (SG) and a fractal-like, turbine-blade roughness (TB).

The large surface scales reduce the overall surface slope if the height statistics (mean height, root-mean-square height, etc.) are kept constant. This leads to several important changes inside the RSL. First, it reduces the occurrence of roughness wakes, which form in regions with high local surface slopes and in turn generate pressure drag and intense mixing-layer turbulence activity. This explains previous observations that the large wavelengths tend to reduce drag generation. Also, the dominance of attached flow over local recirculation regions leads to nontrivial, symmetric quadrant contribution of the dispersive shear stress that averages to nearly zero. As a result, the dispersive momentum flux is negligible, despite intense normal dispersive stresses. In addition, the TKE redistribution to the $v'$ energy appears to be associated with the high-slope surface protuberances, possibly due to the intense form-induced shear and mixing-layer turbulence activity in the wake regions. As a result, the Reynolds-stress anisotropy is enhanced on account of large surface wavelengths, which may explain the good correlation between the roughness drag and the crest-level $v_{\mathrm{rms}}^+$, as widely observed for a wide range of roughness.

The textual effects on various turbulence production mechanisms are also identified. The shear production, $P_s$, peaks near the roughness crest and essentially scales with wall units. In contrast, the individual form-induced productions ($P_m$ and $P_w$) are more texture-sensitive and peak at a lower elevations where form-induced fluctuations are intense. In particular, three textural factors can be identified: (1) The roughness drag coefficient determines the DA momentum in the RSL and subsequently the intensity of form-induced shear that produces turbulence. (2) The roughness geometry function ($\Phi$) is a key factor in the correlation between the wall-normal variations of the spatial-averaged values of Reynolds shear stress and the form-induced shear, affecting $P_m$ as a result. (3) Both small (usually peaky) and large (usually undulatory) surface structures play a role in determining the correlation of the spatial perturbations of Reynolds stresses and mean velocities, which affect the magnitude and even the sign of $P_w$.

In contrast to previous results that suggest negligible $P_w$ and $P_m$ of TKE in the cases of narrow-scale roughness, it is shown here that these production terms can reach magnitudes comparable to the shear production for a multiscale surface. In addition, it is important to analyze the individual production terms despite the fact that their sum appears less texture sensitive as they partially cancel out. This is because, in nonequilibrium flows, these two terms may react differently to imposed

distortions, as the product of two spatial perturbations may behave drastically differently compared to the product of their spatial means. This needs to be clarified in a future investigation.

## ACKNOWLEDGMENTS

[1] M. R. Raupach, R. A. Antonia, and S. Rajagopalan, Rough-wall boundary layers, Appl. Mech. Rev. **44**, 1 (1991).

[2] J. Jiménez, Turbulent flows over rough walls, Annu. Rev. Fluid Mech. **36**, 173 (2004).

[3] J. Yuan and U. Piomelli, Numerical simulation of a spatially developing accelerating boundary layer over roughness, J. Fluid Mech. **780**, 192 (2015).

[4] D. Chen, C. Chen, F.-E. Tang, P. Stansby, and M. Li, Boundary layer structure of oscillatory open-channel shallow flows over smooth and rough beds, Exp. Fluids **42**, 719 (2007).

[5] C. D. Ghodke and S. V. Apte, DNS study of particle-bed–turbulence interactions in an oscillatory wall-bounded flow, J. Fluid Mech. **792**, 232 (2016).

[6] M. Hino, M. Kashiwayanagi, A. Nakayama, and T. Hara, Experiments on the turbulence statistics and the structure of a reciprocating oscillatory flow, J. Fluid Mech. **131**, 363 (1983).

[7] M. R. Raupach and R. H. Shaw, Averaging procedures for flow within vegetation canopies, Bound.-Lay. Meteorol. **22**, 79 (1982).

[8] J. Finnigan, Turbulence in plant canopies, Annu. Rev. Fluid Mech. **32**, 519 (2000).

[9] E. Mignot, E. Barthelemy, and D. Hurther, Double-averaging analysis and local flow characterization of near-bed turbulence in gravel-bed channel flows, J. Fluid Mech. **618**, 279 (2009).

[10] V. Nikora, I. McEwan, S. McLean, S. Coleman, D. Pokrajac, and R. Walters, Double-averaging concept for rough-bed open-channel and overland flows: Theoretical background, J. Hydraul. Eng. **133**, 873 (2007).

[11] J. Yuan and U. Piomelli, Roughness effects on the Reynolds stress budgets in near-wall turbulence, J. Fluid Mech. **760**, R1 (2014).

[12] O. Coceal, T. G. Thomas, I. P. Castro, and S. E. Belcher, Mean flow and turbulence statistics over groups of urban-like cubical obstacles, Bound.-Lay. Meteorol. **121**, 491 (2006).

[13] M. G. Giometto, A. Christen, C. Meneveau, J. Fang, M. Krafczyk, and M. B. Parlange, Spatial characteristics of roughness sublayer mean flow and turbulence over a realistic urban surface, Bound.-Lay. Meteorol. **160**, 425 (2016).

[14] S. Dey and R. Das, Gravel-bed hydrodynamics: Double-averaging approach, J. Hydraul. Eng. **138**, 707 (2012).

[15] K. A. Flack and M. P. Schultz, Review of hydraulic roughness scales in the fully rough regime, J. Fluids Eng. **132**, 041203 (2010).

[16] E. Napoli, V. Armenio, and M. De Marchis, The effect of the slope of irregularly distributed roughness elements on turbulent wall-bounded flows, J. Fluid Mech. **613**, 385 (2008).

[17] A. Sigal and J. E. Damberg, New correlation of roughness density effects on the turbulent boundary layer, AIAA J. **28**, 554 (1990).

[18] P. Orlandi, S. Leonardi, and R. A. Antonia, Turbulent channel flow with either transverse or longitudinal roughness elements on one wall, J. Fluid Mech. **561**, 279 (2006).

[19] O. Coceal, A. Dobre, T. G. Thomas, and S. E. Belcher, Structure of turbulent flow over regular arrays of cubical roughness, J. Fluid Mech. **589**, 375 (2007).

[20] L. Chau and K. Bhaganagar, Understanding turbulent flow over ripple-shaped random roughness in a channel, Phys. Fluids **24**, 115102 (2012).

[21] A. Busse, M. Thakkar, and N. D. Sandham, Reynolds-number dependence of the near-wall flow over irregular rough surfaces, J. Fluid Mech. **810**, 196 (2017).

[22] P. Forooghi, A. Stroh, P. Schlatter, and B. Frohnapfel, Direct numerical simulation of flow over dissimilar, randomly distributed roughness elements: A systematic study on the effect of surface morphology on turbulence, Phys. Rev. Fluids **3**, 044605 (2018).

[23] P. Passalacqua, F. Porté-Agel, E. Foufoula-Georgiou, and C. Paola, Application of dynamic subgrid-scale concepts from large-eddy simulation to modeling landscape evolution, Water Resour. Res. **42**, W06D11 (2006).

[24] W. Anderson and C. Meneveau, Dynamic roughness model for large-eddy simulation of turbulent flow over multiscale, fractal-like rough surfaces, J. Fluid Mech. **679**, 288 (2011).

[25] J. M. Barros, M. P. Schultz, and K. A. Flack, Measurements of skin-friction of systematically generated surface roughness, Int. J. Heat Fluid Flow **72**, 1 (2018).

[26] A. Scotti, Direct numerical simulation of turbulent channel flows with boundary roughened with virtual sandpaper, Phys. Fluids **18**, 031701 (2006).

[27] J. Yuan and U. Piomelli, Numerical simulations of sink-flow boundary layers over rough surfaces, Phys. Fluids **26**, 015113 (2014).

[28] A. Keating, U. Piomelli, K. Bremhorst, and S. Nešić, Large-eddy simulation of heat transfer downstream of a backward-facing step, J. Turbul. **5**, N20 (2004).

[29] V. Nikora, D. Goring, I. McEwan, and G. Griffiths, Spatially averaged open-channel flow over rough bed, J. Hydraul. Eng. **127**, 123 (2001).

[30] A. K. M. F. Hussain, and W. C. Reynolds, The mechanics of an organized wave in turbulent shear flow. Part 3. Theoretical models and comparisons with experiments, J. Fluid Mech. **54**, 263 (1972).

[31] J. Yuan and U. Piomelli, Estimation and prediction of the roughness function on realistic surfaces, J. Turbul. **15**, 350 (2014).

[32] P. S. Jackson, On the displacement height in the logarithmic velocity profile, J. Fluid Mech. **111**, 15 (1981).

[33] D. Pokrajac, L. J. Campbell, V. Nikora, C. Manes, and I. McEwan, Quadrant analysis of persistent spatial velocity perturbations over square-bar roughness, Exp. Fluids **42**, 413 (2007).

[34] H. Cheng and I. P. Castro, Near wall flow over urban-like roughness, Bound.-Lay. Meteorol. **104**, 229 (2002).

[35] M. R. Raupach, A. S. Thom, and I. Edwards, A wind-tunnel study of turbulent flow close to regularly arrayed rough surfaces, Bound.-Lay. Meteorol. **18**, 373 (1980).

[36] R. D. Moser and P. Moin, The effects of curvature in wall-bounded turbulent flows, J. Fluid Mech. **175**, 479 (1987).

[37] M. P. Schultz and K. A. Flack, Reynolds-number scaling of turbulent channel flow, Phys. Fluids **25**, 025104 (2013).

[38] L. I. Langelandsvik, G. J. Kunkel, and A. J. Smits, Flow in a commercial steel pipe, J. Fluid Mech. **595**, 323 (2008).

[39] X. Yang, J. Sadique, R. Mittal, and C. Meneveau, Exponential roughness layer and analytical model for turbulent boundary layer flow over rectangular-prism roughness elements, J. Fluid Mech. **789**, 127 (2016).

[40] V. Nikora, K. Koll, I. McEwan, S. McLean, and A. Dittrich, Velocity distribution in the roughness layer of rough-bed flows, J. Hydraul. Eng. **130**, 1036 (2004).

[41] J. M. Wallace, H. Eckelmann, and R. S. Brodkey, The wall region in turbulent shear flow, J. Fluid Mech. **54**, 39 (1973).

[42] O. Coceal, T. G. Thomas, and S. E. Belcher, Spatial variability of flow statistics within regular building arrays, Bound.-Lay. Meteorol. **125**, 537 (2007).

[43] E. Mignot, D. Hurther, and E. Bartheleemy, On the structure of shear stress and turbulent kinetic energy flux across the roughness layer of a gravel-bed channel flow, J. Fluid Mech. **638**, 423 (2009).

[44] H. Le, P. Moin, and J. Kim, Direct numerical simulation of turbulent flow over a backward-facing step, J. Fluid Mech. **330**, 349 (1997).

[45] E. Mignot, E. Barthélemy, and D. Hurther, Turbulent kinetic energy budget in a gravel-bed channel flow, Acta Geophys. **56**, 601 (2008).

[46] M. K. Chyu and V. Natarajan, Heat transfer on the base surface of three-dimensional protruding elements, Int. J. Heat Mass Transf. **39**, 2925 (1996).

[47] M. Manhart, Vortex shedding from a hemisphere in a turbulent boundary layer, Theor. Comput. Fluid Dyn. **12**, 1 (1998).

[48] R. Martinuzzi and C. Tropea, The flow around surface-mounted, prismatic obstacles placed in a fully developed channel flow, ASME J. Fluids Eng. **115**, 85 (1993).

[49] E. Savory and N. Toy, The flow regime in the turbulent near wake of a hemisphere, Exp. Fluids **4**, 181 (1986).